aerospace

MDPI

Article

Accuracy of Aerodynamically and Structurally Non-Linear Unsteady Vortex Lattice Method for Aeroelastic Prediction in Low-Reynolds Flows

Mindaugas Dagilis *, Martynas Lendraitis and Sigitas Kilikevičius

Department of Transport Engineering, Kaunas University of Technology, Studentu 56, 51424 Kaunas, Lithuania; martynas.lendraitis@ktu.lt (M.L.); sigitas.kilikevicius@ktu.lt (S.K.)
* Correspondence: mindaugas.dagilis@ktu.lt

Abstract

Panel-based aeroelasticity models are commonly used to conduct mid-fidelity aeroelastic analysis. The unsteady vortex lattice method (UVLM) in particular is used when non-linear aerodynamic corrections are needed, for example by utilizing the α-convergence method. While this method is well tested for non-linear corrections in high-Reynolds transonic flows for both steady and unsteady cases, its effectiveness has not been well researched in unsteady low-Reynolds flows. This paper tests the effectiveness of the α-convergence method in this regime by comparing modeling results with original wind tunnel test results. In the steady aeroelastic displacement tests, the aerodynamic non-linearity improved the modeling results significantly, with an error under $\pm 10\%$ at all tested angles of attack, compared to a maximum error of -30.8% for the aerodynamically linear models. In the flutter test case, the aerodynamic non-linearity had less of an impact, with structural non-linearity being more important in this case. However, the maximum flutter speed error for the aerodynamically non-linear model was still lower, at -14.4%, compared to $+19.6\%$ for the aerodynamically linear model.

Keywords: vortex lattice method; non-linear aeroelasticity; flutter; wind tunnel experiment

1. Introduction

Aeroelastic modeling is highly relevant for modern aircraft design and control law development. A variety of aeroelasticity models are used for aircraft design optimization [1–4], flutter suppression system development [5–7], and gust load alleviation system development [8–10]. Many of these applications are highly iterative, and require fast aeroelasticity models in order to be viable without access to very-high-performance computers. Because of this, many authors focus on fast aeroelasticity modeling [11–15], and some of them propose data-driven methods, while others analyze physics-based methods. Generally, data-driven aeroelasticity models have excellent performance, performing calculations much faster than high fidelity physics-based methods, while providing comparable results [13,15]. However, by nature, the data-driven methods require a lot of pre-existing data to develop, and have limited flexibility regarding changing structural or aerodynamic parameters of the structure. These qualities make them well-suited for applications where the analyzed geometry stays constant, such as control law development, but less suitable for variable-geometry applications such as parametric design optimization. In comparison, physics-based methods usually have a higher computational cost for comparable results,

Check for updates

Received: 20 May 2026
Revised: 17 July 2026
Accepted: 20 July 2026
Published: 23 July 2026

 https://doi.org/10.3390/aerospace13080661

but are more flexible, easier to develop for a specific aircraft, and easy to adapt to changing aerodynamic and structural properties.

The computational cost of physics-based methods varies greatly with complexity, with CFD-based methods [2,16,17] generally being the most computationally expensive, panel-based methods (mostly vortex lattice method (VLM) [18–20] and the doublet lattice method (DLM) [21,22]) providing mid-fidelity results at average computational costs, and more traditional strip-based aerodynamic methods [5,23,24] providing excellent computational performance, but with lower accuracy. For many applications, the mid-fidelity panel-based methods provide a good balance between performance and accuracy. DLM is readily applicable to frequency-domain applications and is an industry standard for flutter predictions; however, VLM is more flexible and easier to set up for complex geometries when applied in the time domain. Additionally, while both are inviscid methods, there are many implementations of non-linear VLM, taking viscous [25,26] and compressible [20,27] effects into account, whereas DLM is usually used in the basic linear implementation.

One of the main methods to account for non-linear aerodynamic effects in VLM is the α-convergence method, first described in [28]. It is well established for viscosity and compressibility corrections for VLM, and more suitable for steady cases [1], but has also been successfully applied to unsteady cases such as flutter prediction [27]. However, the existing research mainly focuses on applications of the unsteady version of this method in full-size aircraft analysis at $\mathrm{Re} \geq 1 \times 10^6$. Some research describes the use of the very similar hybrid unsteady vortex lattice-vortex particle method with α-convergence non-linearity correction in the Reynolds number range $27 \times 10^3 \leq \mathrm{Re} \leq 170 \times 10^3$ [29,30]. However, while utilizing an unsteady model, the research focuses on the relatively steady case of a small UAV rotor in hover conditions, and only compares the results with steady experimental measurements.

There is an apparent research gap in evaluating the suitability of the non-linear UVLM with α-convergence correction for unsteady aeroelastic modeling in low-Reynolds flows, especially in relation to experimental results. Because the method only uses steady airfoil lift data for the non-linear aerodynamic corrections, the accuracy for unsteady cases is not guaranteed, and it requires additional validation. This paper focuses on evaluating the effectiveness of this method for both steady and unsteady aeroelastic analysis in the Reynolds number range $41.5 \times 10^3 \leq \mathrm{Re} \leq 100.3 \times 10^3$, comparing the results of the model with original results from wind tunnel testing. Inside this Reynolds number range, the performance of an airfoil can greatly vary even for relatively small changes of Reynolds number [31]. If proven to be reliable in this regime, the non-linear UVLM could be more readily used for aeroelastic design and control law design of small fixed-wing UAVs, as they often operate in this range of Reynolds numbers.

2. Aeroelasticity Model

The core aeroelasticity model is the same as described in an earlier study by the authors [32]. The structural dynamics part of the model is based on Euler beam elements, with an implicit generalized-α time integration scheme and proportional damping. The aerodynamic part is based on UVLM with a ring-vortex deformable wake formulation. Different from the earlier work, the α-convergence method is applied to UVLM in order to account for airfoil lift nonlinearity. In the model description and result overview, the chordwise direction is labeled X, the spanwise direction is Y, and the normal direction is Z.

2.1. Structural Dynamics Model

The structural dynamics of the aeroelasticity model are based on a beam structure of Euler beam elements. The standard stiffness and consistent-mass matrices are used for the beam, with an addition in the mass matrix to account for the inertia moment of the cross-section, the same as in the authors' earlier work [32]. Proportional (Rayleigh) damping is used. In the non-linear version of the structural model, the global stiffness and mass matrices are adjusted based on the angular position of each element (a corotational non-linear approach).

2.2. Aerodynamics Model

The aerodynamic model is based on standard ring-vortex UVLM with a deformable wake [33]. The steady aerodynamic force is evaluated at each bound vortex line of the vortex lattice, and the unsteady force is evaluated at each panel. The α-convergence method is applied to each chordwise strip of the wing at each time-step using the following algorithm [28]:

1. Set adjustment angle $\Delta\alpha = 0$.
2. Solve the regular UVLM equations.
3. Calculate the local steady lift coefficient c_{L3D} for the chordwise strip.
4. Calculate the effective local airfoil angle of attack $\alpha_{2D} = \arcsin\left(\frac{c_{L3D}}{2\pi}\right)$.
5. Lookup the expected airfoil lift coefficient c_{L2D} at α_{2D}.
6. Calculate the new $\Delta\alpha = \alpha_{geom} - \arcsin\left(\frac{c_{L2D}}{c_{L3D}}\sin\left(\alpha_{geom}\right)\right)$.
7. Rotate UVLM panel normals around Y-axis by $\Delta\alpha$.
8. Repeat steps 2–7 until for each strip the local lift coefficient converges $|c_{L3D,i} - c_{L3D,i-1}| < \epsilon$.

For this paper $\epsilon = 10^{-2}$ is used for convergence control. To confirm the validity of this value, a steady aeroelastic displacement analysis is performed using the fully non-linear aeroelasticity model (model D as described at the end of Section 2.3), comparing the results when using values $\epsilon = 10^{-2}$ and $\epsilon = 10^{-3}$. The maximum negative and positive relative differences in wingtip displacement between the two epsilon values are -0.27% and $+0.29\%$, showing that the $\epsilon = 10^{-2}$ value is appropriate and does not significantly impact the accuracy of the model.

2.3. Model of the Test Case Wing

For the wing used in the wind tunnel experiments, described in Section 3.2, the structural properties of the computational model are derived from the main spar properties, and then scaled to match the real wing. The main spar is made of 51CrV4 alloy spring steel, with a tensile modulus of 210 GPa, density of 7800 $\mathrm{kg/m^3}$, and Poisson ratio of 0.30. The cross-section of the spar is rectangular, 40 mm wide and 0.5 mm thick. The resulting cross-sectional properties of the wing spar are given in Table 1. Because the total wing is both heavier and stiffer than just the spar, additional adjustment ratios were introduced to adjust some structural properties of the wing. The adjustment ratios and the resulting structural parameters of the full wing are also given in Table 1. The adjustment ratios for the out-of-plane (OOP) bending stiffness and torsional stiffness are determined based on static structural tests of the manufactured wing model, the mass adjustment ratio is calculated by weighing the manufactured wing, and the Y-rotational inertia adjustment ratio is determined from the inertial properties of the CAD model of the wing. Additionally, to account for the deformations at the clamping point of the wing, a 3 mm long part of the main spar is added to the structural model at the wing root (it is omitted from aerodynamic calculations); this additional part uses the structural properties of the wing spar cross-section, without the adjustment ratios applied.

Table 1. Cross-section properties of the wing spar, and adjusted properties for the full wing.

Parameter	Wing Spar Cross-Section	Adjustment Ratio	Total Wing Cross Section
Axial stiffness EA	4.2×10^6 N	1.00	4.2×10^6 N
OOP bending stiffness EI_{xx}	8.75×10^{-2} Nmm^2	2.19	1.92×10^{-1} Nmm^2
IP bending stiffness EI_{zz}	5.6×10^2 Nmm^2	1.00	5.6×10^2 Nmm^2
Torsional stiffness GI_{yy}	1.35×10^{-1} Nmm^2	2.95	3.98×10^{-1} Nmm^2
Mass ρA	1.56×10^{-1} kg/m	1.38	2.15×10^{-1} kg/m
X-rotational inertia ρI_{Ixx}	3.25×10^{-9} kgm	1.00	3.25×10^{-9} kgm
Y-rotational inertia ρI_{Iyy}	2.08×10^{-5} kgm	1.57	3.27×10^{-5} kgm
Z-rotational inertia ρI_{Izz}	2.08×10^{-5} kgm	1.00	2.08×10^{-5} kgm

Some elements are added to the model as point masses, shown in Table 2. The accelerometers, their amplifier and holder are modeled as a pure point mass, and the threaded wingtip rod and extra weights are modeled as an extra mass with rotational inertia (although the rotational inertia around the X-axis is neglected). The masses are determined by weighing the components, the rotational inertia of the threaded rod is calculated using the equation for a thin rod rotating around its center (with a length of 100 mm), and the inertia of the extra weights is calculated using the equation for two point masses rotating around their central point (with the distance to the rotation axis equal to 46 mm).

Table 2. Point masses added to the aeroelastic model.

Component	Spanwise Position, m	m, kg	I_X, kgm^2	I_Y, kgm^2	I_Z, kgm^2
Accelerometers, amplifier, holder	0.316	0.0058	0.0	0.0	0.0
Wingtip rod	0.330	0.0070	0.0	5.83×10^{-6}	5.83×10^{-6}
Wingtip weights	0.330	0.0106	0.0	2.24×10^{-5}	2.24×10^{-5}

For the aerodynamic model, the wing is split into 8 chordwise and 16 spanwise elements, distributed uniformly. For the aerodynamically linear model with no corrections applied, the effective airfoil lift slope is $C_L = 2\pi$, equivalent to the thin-airfoil case. The airfoil lift curve for the α-convergence method is shown in Figure 1; it is based on experimental results at Re $= 80 \times 10^3$ from [31]. Based on these experiments, at low angles of attack, the airfoil has a lift slope steeper than 2π, resulting in more lift than in the aerodynamically linear, inviscid case.

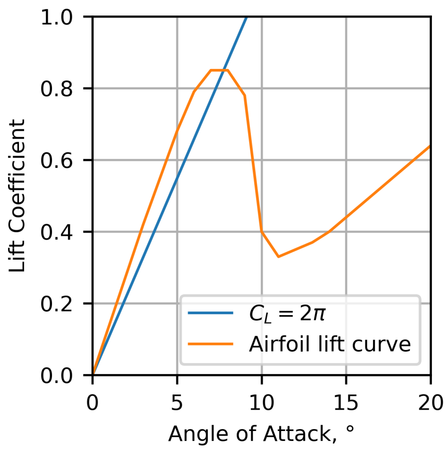

Figure 1. Airfoil lift curve used for the non-linear aeroelastic modeling, compared with the linear $C_L = 2\pi$ lift model.

To evaluate the importance of structural and aerodynamic non-linearity for the analyzed test case, four configurations of the aeroelasticity model are evaluated:

1. Model A—structurally and aerodynamically linear.
2. Model B—structurally linear, aerodynamically non-linear.
3. Model C—structurally non-linear, aerodynamically linear.
4. Model D—structurally and aerodynamically non-linear.

The structurally linear models (A and B) use a constant stiffness matrix that does not change when the structure is deformed, and for the non-linear models (C and D), the element stiffness matrices are rotated based on the local angular displacement before being added to the global stiffness matrix. The aerodynamically linear models (A and C) use standard UVLM, and the non-linear models (B and D) use the α-convergence method as described in Section 2.2. Even for case A, the complete aeroelastic model is not completely linear, because of the two-way coupling between the aerodynamic and structural models.

2.4. Computational Flutter Detection

The implemented unsteady aeroelasticity model works in the time domain, and because of this, the flutter speed cannot be directly computed by the model. In order to determine the flutter speed and obtain the computational results presented in Section 4.2, a separate flutter detection script was used as a wrapper for the aeroelasticity model.

It begins by running the model at an initial guess of flutter speed for 0° angle of attack, obtaining a steady-state solution, then introducing a disturbance exciting the 2OOP (second out-of-plane bending) mode. The excitation is achieved by adding a 1.0 N out-of-plane force at the half-span and a -0.5 N out-of-plane force at the wingtip for a duration of 10^{-3} s. The model then continues to run for 0.7 s of model time, after which an automated FFT analysis is used to determine if the 2OOP mode has an increasing or a decreasing amplitude. If the amplitude is increasing, the script registers that flutter is happening at this speed, and repeats the test case with decreasing flow speeds in 0.1 m/s increments, until flutter stops, which is then noted as the flutter boundary for that angle of attack. If initially flutter does not develop, the speed is instead increased in the same increments until flutter is reached, and this is noted as the flutter boundary. After detecting the flutter boundary for the current angle of attack, the angle of attack is increased by 0.1° and the process is repeated, using the previous flutter speed as the initial guess.

While this flutter detection procedure might overlook the development of 1OOP (first out-of-plane bending) flutter, a preliminary manual modeling run of different test cases spanning the full range of tested angles of attack indicates that this flutter mode is not present in the modeling results. Because of this, the 2OOP excitement technique was chosen instead of a 1OOP excitement. A manual review of some of the automated modeling cases confirms that the script successfully identifies the cases where no flutter is present and that they are true negatives, rather than cases of different flutter modes (1OOP or 3OOP) that the script fails to detect.

3. Experimental Methodology

Aeroelasticity experiments were performed in a wind tunnel in order to validate the developed aeroelastic model. During the experiments, a specially made wing was tested at a set of different angles of attack and flow speeds. The wingtip displacements were measured to determine the steady aeroelastic displacement of the wingtip. Additionally, accelerations were measured at the wingtip in order to determine the aeroelastic modal properties of the wing.

3.1. Wind Tunnel

For the experiments, the wind tunnel at the Lithuanian Energy Institute is used. The wind tunnel is of closed return type, with an open test subsection. The diameter of the tunnel at the test subsection is 400 mm, and the maximum achieved airflow speed is 40 m/s. An ultrasound-based airspeed sensor is installed in the tunnel for speed measurement.

3.2. Wind Tunnel Model

The wind tunnel model used for experiments is a rectangular planform wing with a half-span of 324 mm and a chord of 50 mm. A drawing of the wind tunnel model is shown in Figure 2. The symmetrical NACA 0018 airfoil is used for the wing.

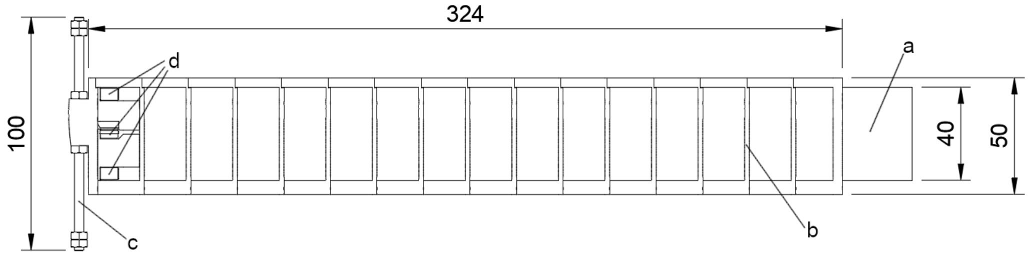

Figure 2. Drawing of the used wind tunnel model with main dimensions shown. a—wing spar section used for cantilever mounting, b—wing rib with leading and trailing edge extensions, c—wingtip rod for attaching extra mass, and d—accelerometers.

The main structural element of the wing is a steel spar. The spar is made out of hot-rolled 51CrV4 alloy spring steel. The thickness of the spar is 0.5 mm, and the width is 40 mm. It extends from the root of the wing up to 308 mm from the root, leaving the last 16 mm of the wing without the spar. The wing spar also extends 32 mm past the root of the wing; this part is clamped to mount the wing (Figure 2, a).

Wing ribs (Figure 2, b) are mounted on the wing spar to create the outer aerodynamic shape of the wing. The wing ribs are 3D-printed out of PCTG plastic. The ribs are positioned every 20 mm along the span of the wing, with 14 regular ribs in total, and one thicker rib at the wing root. The main ribs are 2 mm thick, with a hole for routing sensor wires. The rib at the root of the wing is 4 mm thick. At the leading and trailing edge of each rib is a spanwise extension that extends to the next rib, in order to make the leading and trailing edge shape more consistent along the span. The wingtip rib is replaced with a plastic housing for accelerometers, with an additional hole for mounting a threaded rod (Figure 2, c), used to attach additional masses at the wingtip.

Three accelerometers are mounted at the wingtip (Figure 2, d), as well as a PCB amplifier, described in more detail in Section 3.3.

The wing is covered with a thin heat-shrink film, providing the outer aerodynamic shape.

At the wingtip, a 100 mm long M4 threaded rod is attached (Figure 2, c), with a mass of 7.0 g. The rod is centered at the mid-chord of the wing. At the tips of the rod (46 mm from the mid-chord), additional masses are attached, which are 5.3 g each.

An overview of the mass properties of the wing is provided in Table 3. The total mass of the wing spar is 52.8 g. A 32 mm long part of the wing spar extending out of the root of the wing is used to mount it, and is not part of the unsupported mass of the wing. The mass of this mounting part is 5.0 g, leaving the unsupported mass of the spar equal to 47.8 g. The 14 regular wing ribs have a total mass of 12.2 g (average of 0.87 g per wing rib), and the thicker wing rib at the root has a mass of 1.2 g. The accelerometer housing has a mass of 5.3 g. The total mass of all 3D printed parts is 18.7 g. The accelerometers have a manufacturer-specified mass of 0.28 g, giving a total mass of 0.8 g (rounded) for three of them. The amplifier PCB with all soldered components has a mass of 2.4 g, and the accelerometer wires have a total mass of 0.4 g. These components make the total unsupported mass of the wing without adhesives and skin equal to 87.7 g (including the wing tip rod and extra weights). The measured mass of the assembled wing is 98.1 g, making the total unsupported mass 93.1 g.

Table 3. Mass components of the wind tunnel model (for the wing spar, only the unsupported mass is included).

Component	Mass, g
Wing spar	47.8
Wing ribs	13.4
Accelerometer housing	5.3
Accelerometers	0.8
Amplifier	2.4
Wires	0.4
Skin and adhesive	5.4
Wingtip rod	7.0
Wingtip masses	10.6
Total	93.1

At the root of the wing, a round steel plate is mounted to act as the aerodynamic ground plane. The diameter of the plate is 240 mm.

3.3. Measurement Setup

One laser triangulation distance measurement sensor and three uni-directional accelerometers are used to perform the measurements during the wind tunnel experiment.

The laser triangulation sensor is mounted externally and is used to measure the displacement of the wingtip in the normal direction. A Micro-Epsilon optoNCDT-1220 sensor (Micro-Epsilon Messtechnik GmbH, Ortenburg, Germany) is used, with a measurement range of 100–600 mm. The sensor has a specified linearity error of less than 1.5 mm, or 0.30% of the full scale output, and a specified repeatability of 0.05 mm. The analog output mode of the sensor is used, in order to have the measurement synchronized with the analog accelerometers. The digital readout is used to check the validity of the analog output.

The accelerometers are mounted 9.5 mm from the wingtip. Two are mounted at the leading and the trailing edge to measure OOP accelerations, and the third one is mounted at the mid-chord and situated to measure in-plane accelerations. Knowles BU-23173 piezo-ceramic accelerometers (Knowles Corporation, Itasca, IL, USA) are used, chosen for their low mass equal to 0.28 g. The accelerometers can measure accelerations of up to 100 $\mathrm{m/s^2}$, and have a relatively constant specified sensitivity in the 30–3000 Hz range (the manufacturer does not provide sensitivity data at lower frequencies). The nominal sensitivity is 0.2 $(\mathrm{m/s^2})/\mathrm{mV}$ according to manufacturer data. This sensitivity value was checked by comparing the acceleration and displacement measurement data, and appears to be accurate.

A three-channel amplifier is mounted on the wingtip to amplify the accelerometer signal close to the source. The amplifier uses the LM2902PT four-channel operational amplifier (STMicroelectronics NV, Geneva, Switzerland), and is setup in an inverting configuration, with an integrated band-pass filter. The amplification factor of each channel is 10, the -3 dB high-pass cutoff is 0.034 Hz, and the low-pass cutoff is 340 Hz. The total mass of the amplifier is 2.4 g.

A DaqBook/2020 digital acquisition system (Measurement Computing Corporation, Norton, MA, USA) is used to capture the data from all four sensors. The system has a 16-bit analog-to-digital converter, and a maximum sampling rate of 200 kHz (split between all active channels). It has an integrated adjustable amplifier with a maximum gain of 64, and an input voltage range of −10 V to +10 V. For this experiment, internal amplification is disabled, and a 5 kHz sampling rate is used.

3.4. Test Cases

The wind tunnel testing is performed at angles of attack between 0° and 10°, with a step of 2.5°. After setting each angle of attack, the laser triangulation sensor is repositioned to measure the wingtip deflections in the normal direction. At each angle of attack, the flow speed is set at 11.8 m/s (the minimum possible in the wind tunnel without adding a mesh), then increased to 14 m/s, and further in 2 m/s intervals. At 0°, the interval is initially increased, because flutter is only expected at higher speeds. In all cases, the interval is reduced if the wing appears to approach flutter. When flutter is reached, the flow speed is slowly decreased, stopping the flutter with a manual flutter brake each time, until flutter no longer develops. At each speed, a 20 s long acceleration and displacement sample is measured. At low speeds, the wing is impacted during measurement to induce vibrations; at higher speeds, this was unnecessary because of vibrations induced by wind tunnel turbulence. Each tested angle of attack and flow speed combination is shown in Table 4. With a minimum speed of 11.8 m/s and a maximum of 28.5 m/s, the Reynolds number during testing varied between 41.5×10^3 and 100.3×10^3.

Table 4. Angle of attack–flow speed combinations tested in the wind tunnel.

Angle of Attack, °	Flow Speeds, m/s									
0.0	11.8	14.0	20.0	24.0	26.0	28.0	28.3	28.5		
2.5	11.8	14.1	16.0	18.0	20.1	22.1	23.0	24.0	24.6	25.1
5.0	11.8	14.0	16.0	18.0	20.0	21.0	22.0	22.5		
7.5	11.8	14.2	16.0	18.1	20.0	22.0	24.0	26.0		
10.0	11.8	13.0	15.0	15.8	17.3	19.0	21.0	23.0		

4. Results

In this section, a numerical comparison of the experimental and modeling results is provided, without providing author opinions or possible explanations for the observed results. A more in-depth analysis of the results, including author opinions about the causes of some of the results, is provided in the Discussion (Section 5).

4.1. Steady Aeroelastic Displacement Analysis

The average displacement at different angles of attack and flow speeds is shown in Figure 3 (plotted against dynamic pressure). As expected, the plot shows a near-linear relation between the dynamic pressure of the flow and wingtip displacement. The highest non-linearity is seen at 0° angle of attack, caused by an adjustment of the angle of attack at high speeds in an attempt to get closer to the real aerodynamic zero angle. Before the adjustment, displacements of up to 7.0 mm can be seen. In the other cases, the deviation from a linear relationship is lower, and the lowest deviation is seen at 5°. The highest measured displacement was equal to 128.4 mm, or 39.6% of the half-span of the wing.

The slope of the linear fit lines in Figure 3 is increasing with increasing angle of attack, but the increase is non-linear. The change of the slope with angle of attack is plotted in Figure 4. Because the tip displacement appears to have a nearly linear dependence on aerodynamic force based on Figure 3, the non-linearity present in Figure 4 shows that the dependence of aerodynamic force on angle of attack in these test cases is non-linear. While the wing does not appear to reach its critical angle of attack, a deviation from the linear lift slope region is clearly seen at 7.5° and 10° angles of attack.

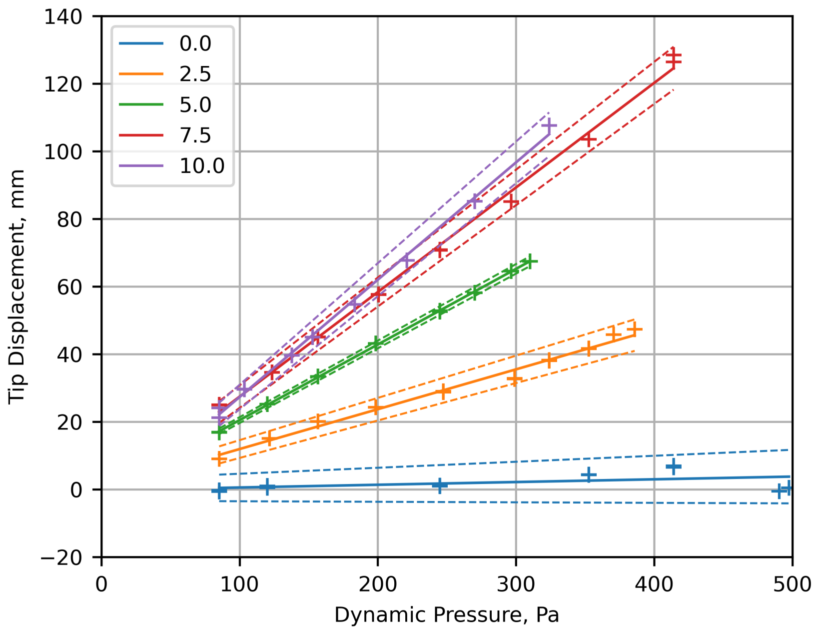

Figure 3. Wingtip displacement change with dynamic pressure at different angles of attack. The linear fit for each angle of attack is shown with solid lines, and the dashed lines show a ±95% fit confidence interval.

The modeling results for steady aeroelastic displacement are shown in Figure 5. It can be seen that, especially at low displacements, aerodynamic non-linearity has a bigger influence than structural non-linearity, as both aerodynamically linear models A and C provide very similar results. The same can be said for the aerodynamically non-linear models B and D. When comparing models A and B (both structurally linear), or C and D (both structurally non-linear), a much larger difference is seen. However, at larger displacements, the structurally non-linear models start showing a larger difference in results to the structurally linear models, with the non-linear models providing lower displacement results. The experimental data appear to be closer to the structurally linear results at all angles of attack, but most noticeably at 7.5° and 10°.

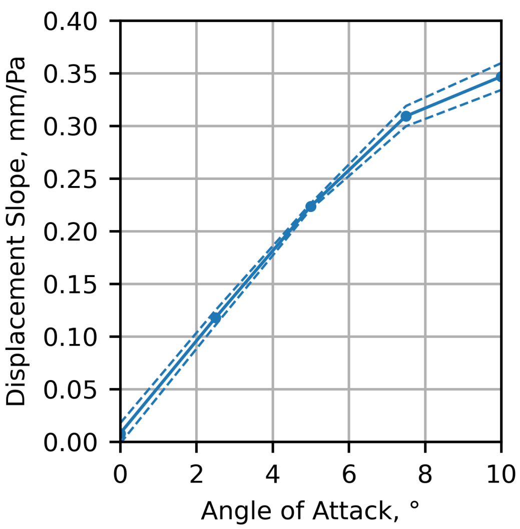

Figure 4. The change of the tip displacement slope with angle of attack. The displacement slopes are from the linear fits shown in Figure 3, and the dashed lines show a ±95% fit confidence interval.

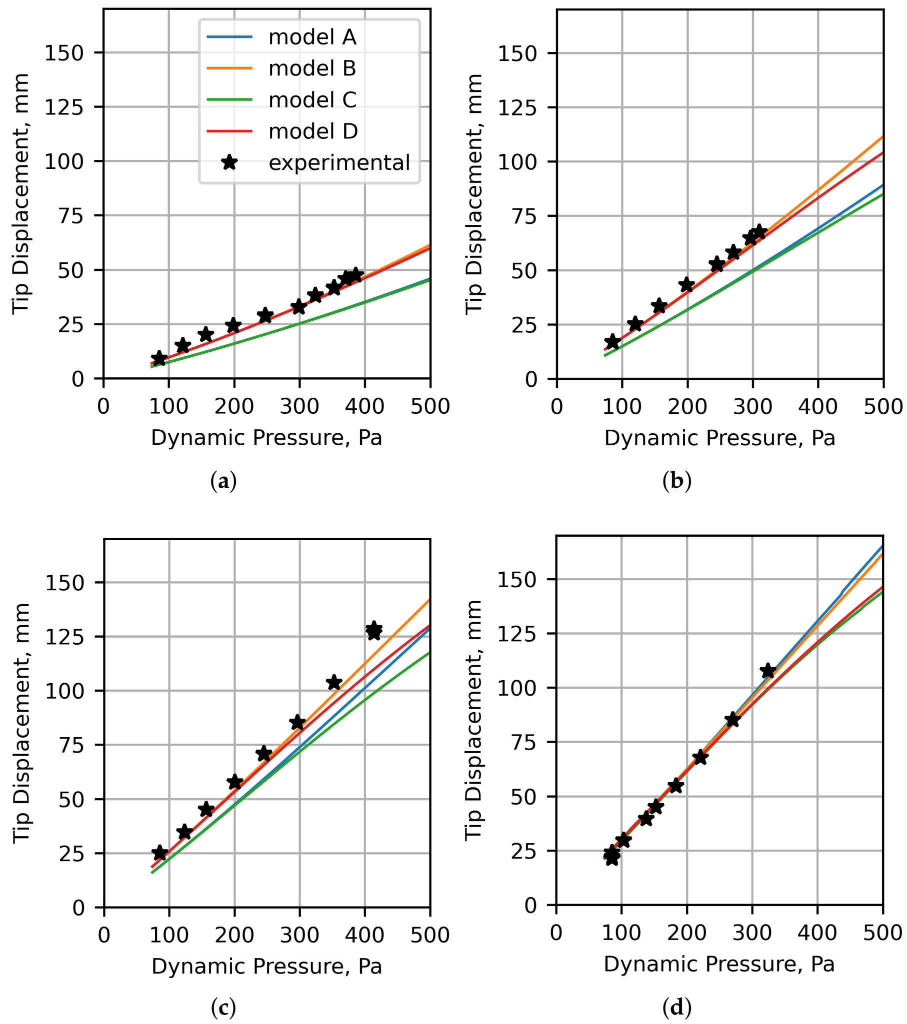

Figure 5. Steady aeroelastic tip displacement results, model comparison to experimental data. (**a**) 2.5°, (**b**) 5.0°, (**c**) 7.5°, and (**d**) 10°.

The errors of steady aeroelastic displacements are shown in Figure 6 and Table 5. It can be seen that the aerodynamically non-linear models B and D both provide good results, only exceeding ±20% error at two points in the 2.5° case, and two points at very low dynamic pressure in the 10° case. In comparison, at 2.5° and 5°, the aerodynamically linear model A and C errors are never under −20%. At 7.5°, they get more similar results to the aerodynamically non-linear models, and at 10°, the results between all models become very similar. Structurally linear models A and B provide lower average errors than their structurally non-linear counterparts C and D at all angles of attack, except for 10°.

Table 5. Average error of each model at each angle of attack.

	Average Displacement Error, %				
Model	**2.5°**	**5.0°**	**7.5°**	**10.0°**	**Overall**
A	−30.6	−25.2	−18.5	+6.9	−16.7
B	−9.0	−6.0	−7.5	+8.7	−3.5
C	−30.8	−25.7	−20.0	+5.6	−17.7
D	−9.5	−7.0	−9.2	+7.9	−4.5

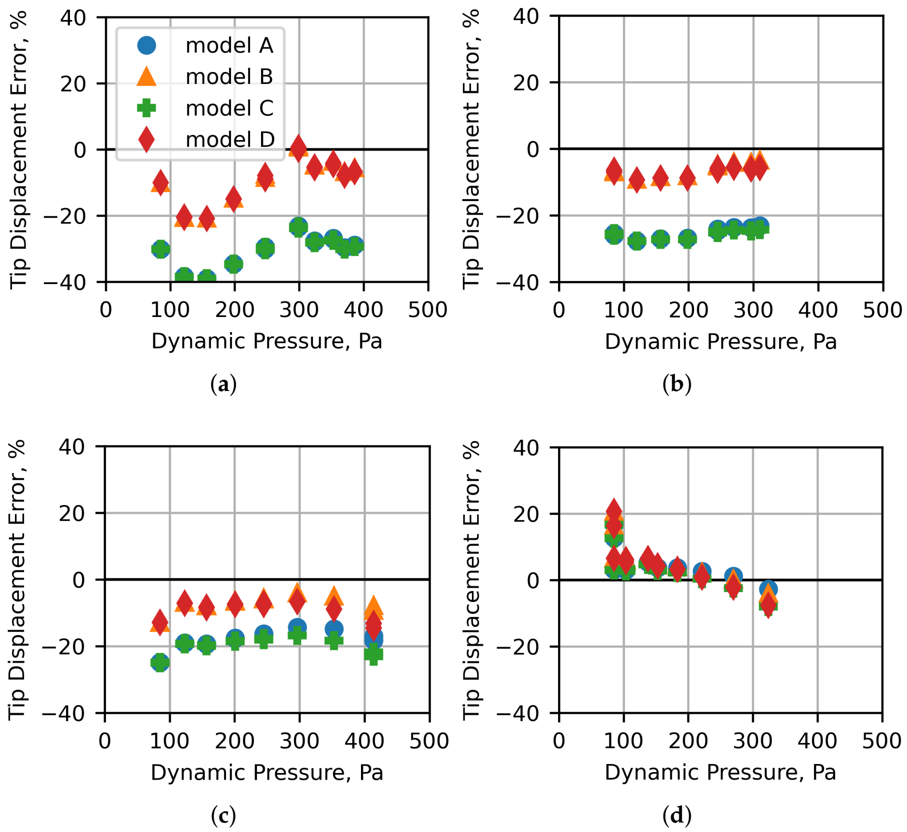

Figure 6. Steady aeroelastic tip displacement model relative error compared to experimental data. (**a**) 2.5°, (**b**) 5.0°, (**c**) 7.5°, and (**d**) 10°.

4.2. Flutter Analysis

By observing the wing at each angle of attack and analyzing the accelerometer data, the flutter speeds for each angle of attack are determined. In most cases, the flutter behavior consisted of the coupled 2nd OOP (2OOP) bending and 1st torsion modes (this flutter mode will be referred to as 2OOP flutter). At 10° angle of attack, a flutter mode coupling 1st OOP bending and 1st torsion modes (1OOP flutter) is also observed, starting much earlier than the flutter at other angles. At higher flow speeds, the wing transitioned from 1OOP to 2OOP flutter. 1OOP flutter was not observed in any modeling results.

The change of the 2OOP flutter speed with angle of attack during the experiment is shown in Table 6 and Figure 7. As expected, the flutter speed decreases with increasing angle of attack. At higher angles of attack, the wing deflection is increased, which creates a strong coupling of the in-plane bending and torsion modes, effectively reducing torsional stiffness. This causes the wing to flutter at a lower speed than without deflection. Interestingly, the flutter speed reduction is especially sudden when the angle of attack increases from 7.5° to 10°. This might be caused by the already present 1OOP flutter at this angle of attack, or by the stronger lift non-linearity near stall. The reduced frequency at flutter onset ranged from 0.144 to 0.233, falling outside the range where the aerodynamics can be considered quasi-steady.

The comparison between experimental and modeling results is shown in Figures 7 and 8. The decrease in flutter speed with increasing angle of attack is correctly captured by both structurally non-linear models (C and D). The aerodynamic non-linearity does not appear to have a very strong effect in this case, with C and D showing relatively similar results. However, both models C and D appear to fail to capture the more sudden drop in flutter speed at 10°. Although the error for model C at 10° is only +1.2%, the calculated flutter speed decreases gradually and shows no sudden decrease at this angle of attack. Model C error ranges starts at +19.6%, then gradually decreases and goes negative, reaching −13.0% at −7.5°, then going to +1.2% at 10°. Model D error starts lower, at +1.8%, then also gradually decreases, reaching −14.4% at −7.5°, then going to +10.9% at 10°.

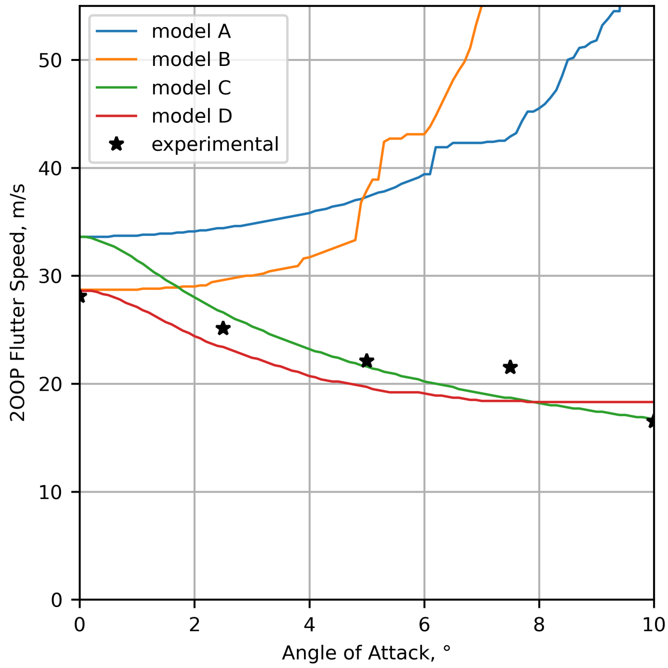

Figure 7. Experimental and modeling 2OOP flutter results.

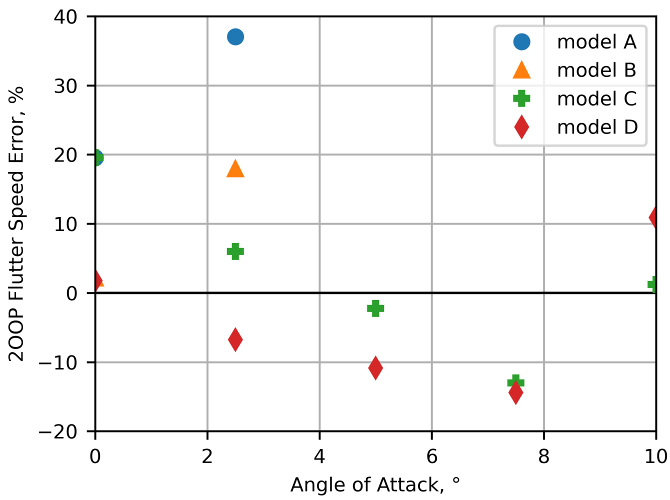

Figure 8. Modeling flutter speed errors compared to experimental results.

Table 6. 2OOP flutter speeds measured during the wind tunnel experiment.

Angle of Attack	2OOP Flutter Speed, m/s	Flutter Frequency at Onset, Hz	Reduced Frequency at Flutter Onset
0.0°	28.1	25.8	0.144
2.5°	25.1	24.8	0.155
5.0°	22.1	25.1	0.178
7.5°	21.5	24.4	0.178
10.0°	16.5	24.5	0.233

The structurally linear models (A and B) both have much higher errors than the structurally linear models at higher angles of attack. As expected, the results at 0° are nearly identical to the corresponding structurally non-linear models, but as the angle of attack increases, the structurally linear models both predict an increase in flutter speed, rather than the experimentally observed decrease. At 5°, both models A and B have a flutter speed error greater than +50%, and it further increases with angle of attack.

5. Discussion

The analyzed steady aeroelastic displacement and flutter cases highlight the necessity for both aerodynamic and structural non-linearity when modeling low-Reynolds, high-displacement aeroelastic cases with a UVLM-based aeroelasticity model.

In the steady aeroelastic displacement case, the aerodynamically non-linear models B and D provide much better results than the aerodynamically linear models A and C. For models B and D, the average displacement error is within the ±10% range for all angles of attack, whereas for models A and C, the maximum average error is −30.6% and −30.8%, respectively. The highest error for models A and C is seen at 2.5°, caused by the lower lift slope in the aerodynamically linear model at low angles of attack. At higher angles, the lift slope of the aerodynamically non-linear model decreases, making the results more similar to the aerodynamically linear models which have a constant lift slope of 2π. It can be concluded that in low-Reynolds flows, aerodynamic non-linearity is important for steady aeroelasticity modeling, even at low angles of attack.

Interestingly, structural non-linearity appears to have a relatively minor impact on steady aeroelastic deflection prediction, with the structurally linear model B actually providing slightly more accurate results than the structurally non-linear model D, even at the highest experimentally measured displacements. With the highest measured displacement equal to 39.6% of the half-span of the wing, a stronger non-linearity of the experimental displacement results could be expected. One possible explanation would be that the increased Reynolds number at higher dynamic pressures increases the lift for the given angle of attack, compensating for the decrease of displacement due to structural non-linearity. At 7.5°, this effect appears to be the strongest, with the displacement growing even faster than the expected linear relationship.

In the flutter case, the structurally non-linear models C and D show superior performance to the structurally linear models A and B. For model C, the predicted flutter speed always stayed within ±20% when compared to the experiment, and for model D, it always stayed within ±15%. The aerodynamic non-linearity appears to play a less important role in this case, mostly reducing the flutter speed in models B and D for the 0° angle of attack. This is most likely caused by the increased airfoil lift slope at low angles of attack, creating a stronger coupling between wing torsion and the produced lift. Models C and D both appear to overestimate the decrease in flutter speed as the angle of attack increases from 0° to moderate angles, with model C having a more significant decrease than model D. Generally, model D appears to follow the decreasing flutter speed curve for angles of attack 2.5° to 7.5° quite well, with a relatively constant negative error, giving somewhat conservative results. Model C intersects the experimental flutter speed curve in this region, so even though the average error is lower, the nature of the flutter speed change is not as close to the experimental results. The fact that both models C and D fail to capture the sudden flutter speed drop at 10° might indicate that this sudden drop is caused by other non-linear effects, and not the change in airfoil lift slope, and a more sophisticated aerodynamic model might be needed to capture it accurately.

The structurally linear models A and B completely fail to predict the change of flutter speed as the wing deforms. This does not mean that traditional linear flutter models would produce equally bad results for this case. For most of them, the flutter speed stays constant with angle of attack, and while in this case, this would significantly over-predict the flutter speed at increasing angles of attack, it would still provide significantly more accurate results than models A and B. This shows that when using an aeroelastic model based on UVLM in high-deflection cases, the structural non-linearity is necessary for accurate flutter speed predictions.

The aerodynamically non-linear models B and D provide higher accuracy at 0° than A and C. This indicates that for low-Reynolds flows (even at low deflections), it can be important to account for the increased airfoil lift slope in order to produce accurate flutter results. Model D in particular seems to follow the changes in flutter speed the best out of all models, so while the differences between models C and D are not major, taking aerodynamic non-linearity into account appears to somewhat improve the flutter prediction results.

Overall, the fully non-linear model D appears to provide the best overall results, giving adequate accuracy in both the steady aeroelastic displacement and flutter cases. The structurally non-linear, aerodynamically linear model C has similarly good results in the flutter case, but much poorer accuracy in the steady aeroelastic displacement case, especially at low angles of attack. The aerodynamically non-linear, structurally linear model B actually provides the best accuracy in the steady aeroelastic displacement case, but is completely inadequate for flutter prediction, giving the worst results out of all models as the angle of attack increases. Finally, the fully linear model A performed the worst, proving completely inadequate for flutter modeling, and giving similarly poor results to model C in the steady aeroelastic displacement case.

The overall results highlight the importance of taking into account both structural and aerodynamic non-linearity for low-Reynolds, high-deflection aeroelastic modeling using UVLM, with the structural non-linearity being more important for accurate flutter prediction, and the aerodynamic non-linearity having more influence on steady aeroelastic displacements. The results show that the α-convergence method for non-linear corrections of UVLM is suited for use in the low Reynolds number range for unsteady aerodynamics with a reduced frequency of up to 0.233, which was the highest tested in this paper.

6. Conclusions

This paper analyzes the effectiveness of an aeroelasticity model based on the non-linear unsteady vortex lattice method with α-convergence in unsteady low-Reynolds flows by comparing the results of the model with both steady (aeroelastic deflection) and unsteady (flutter onset) experimental wind tunnel test cases. The results highlight the suitability of the model for the analyzed Reynolds number range in moderately unsteady flow conditions. The non-linear model provides better results than an aeroelasticity model based on the linear unsteady vortex lattice method in both steady and unsteady cases, with a more significant result improvement in the steady aeroelastic deflection case. The effects of geometric structural non-linearity are also analyzed, with a structurally non-linear model providing significant improvements in the flutter onset test case, but no significant improvement in the steady deflection case, even at very high wingtip deflection values.

The results highlight the requirement of both aerodynamic and structural non-linearity in aeroelastic models that are used to model low-Reynolds, high-deflection cases. While the current work limits the range of tested angles of attack to 10°, the authors intend to expand this range in future work, testing the usefulness of the analyzed non-linear aeroelasticity model in predicting stall flutter and other high-angle aeroelastic phenomena.

Author Contributions: Conceptualization, M.D., M.L. and S.K.; methodology, M.D. and M.L.; software, M.D.; validation, M.L.; formal analysis, M.D.; investigation, M.D., M.L. and S.K.; resources, M.L. and S.K.; data curation, M.D.; writing—original draft preparation, M.D.; writing—review and

editing, M.L. and S.K.; visualization, M.D.; supervision, S.K.; project administration, S.K.; funding acquisition, S.K. All authors have read and agreed to the published version of the manuscript.

Funding: This project has received funding from the Research Council of Lithuania (LMTLT), Agreement No. S-MIP-24-44.

Data Availability Statement: The original data presented in the study are openly available in Zenodo at https://doi.org/10.5281/zenodo.20310799.

Conflicts of Interest: The authors declare no conflicts of interest.

References

1. Parenteau, M.; Laurendeau, E.; Carrier, G. Combined high-speed and high-lift wing aerodynamic optimization using a coupled VLM-2.5D RANS approach. *Aerosp. Sci. Technol.* **2018**, *76*, 484–496. [CrossRef]
2. Voß, A.; Klimmek, T. Parametric aeroelastic modeling, maneuver loads analysis using CFD methods and structural design of a fighter aircraft. *Aerosp. Sci. Technol.* **2023**, *136*, 108231. [CrossRef]
3. Dimitriadis, G. A review of fast unsteady aerodynamic and aeroelastic calculation methods for subsonic aircraft design. *Int. J. Heat Fluid Flow* **2026**, *119*, 110327. [CrossRef]
4. Saporito, M.; Da Ronch, A.; Bartoli, N.; Defoort, S. Robust multidisciplinary analysis and optimization for conceptual design of flexible aircraft under dynamic aeroelastic constraints. *Aerosp. Sci. Technol.* **2023**, *138*, 108349. [CrossRef]
5. Kratochvíl, A.; Valenta, J. Active flutter suppression for light sport aircraft by a control surface split. *CEAS Aeronaut. J.* **2024**, *15*, 977–998. [CrossRef]
6. Ribeiro, F.A.; Geronel, R.S.; De Marqui Junior, C.; Bueno, D.D. An efficient approach to design robust controllers for active flutter suppression. *J. Sound Vib.* **2025**, *617*, 119296. [CrossRef]
7. Vindigni, C.R.; Mantegna, G.; Orlando, C.; Alaimo, A. Simple adaptive wing-aileron flutter suppression system. *J. Sound Vib.* **2024**, *570*, 118151. [CrossRef]
8. Ahmadi, M.; Farsadi, T.; Haddad Khodaparast, H. Enhancing gust load alleviation performance in an optimized composite wing using passive wingtip devices: Folding and Twist approaches. *Aerosp. Sci. Technol.* **2024**, *147*, 109023. [CrossRef]
9. Gao, W.; Liu, Y.; Li, Q.; Lu, B. Gust load alleviation of a flexible flying wing with linear parameter-varying modeling and model predictive control. *Aerosp. Sci. Technol.* **2024**, *155*, 109671. [CrossRef]
10. Pourtakdoust, S.H.; Khodabakhsh, A.H. A deep learning density shaping model predictive gust load alleviation control of a compliant wing subjected to atmospheric turbulence. *Aerosp. Sci. Technol.* **2026**, *168*, 111214. [CrossRef]
11. Cea, A.; Palacios, R.; Iorga, L. Near-Real-Time Nonlinear Analysis of Free-Flying Flexible Aircraft on Modern Hardware Architectures. *AIAA J.* **2026**, *64*, 969–982. [CrossRef]
12. Xia, C.; Wu, P.; Wang, Z. Hybrid deep neural network-validated simulation for aeroelastic control and energy harvesting in piezoelectric structures with adaptive shunt networks. *Aerosp. Sci. Technol.* **2025**, *166*, 110582. [CrossRef]
13. Shi, X.; Gao, C.; Liu, K.; Zhang, W. Transonic aeroelastic stability analysis of launch vehicles using reduced-order model. *Aerosp. Sci. Technol.* **2026**, *168*, 110884. [CrossRef]
14. Su, W.; Song, W. A real-time hybrid aeroelastic simulation platform for flexible wings. *Aerosp. Sci. Technol.* **2019**, *95*, 105513. [CrossRef]
15. Das, A.; Marzocca, P.; Coppotelli, G.; Levinski, O.; Taylor, P. A data-driven approach for rapid detection of aeroelastic modes from flutter flight test based on limited sensor measurements. *Mech. Syst. Signal Process.* **2024**, *220*, 111712. [CrossRef]
16. Hermes, A.; Zahle, F.; Riva, R.; Madsen, J.; Bergami, L.; Skovby, C. High fidelity aeroelastic stability analysis of operating wind turbines. *Renew. Energy* **2025**, *253*, 123424. [CrossRef]
17. Woodgate, M.A.; Barakos, G.N. High fidelity CFD/CSD method for rotor blade optimization. *Aerosp. Sci. Technol.* **2026**, *174*, 111895. [CrossRef]
18. Campagna, D.; Gulizzi, V.; Benedetti, I. A DG-VLM framework for computational static aeroelastic analysis of composite wings. *Compos. Struct.* **2025**, *353*, 118697. [CrossRef]
19. Gulizzi, V.; Benedetti, I. Computational aeroelastic analysis of wings based on the structural discontinuous Galerkin and aerodynamic vortex lattice methods. *Aerosp. Sci. Technol.* **2024**, *144*, 108808. [CrossRef]
20. Parenteau, M.; Laurendeau, E. A general modal frequency-domain vortex lattice method for aeroelastic analyses. *J. Fluids Struct.* **2020**, *99*, 103146. [CrossRef]
21. Vindigni, C.R.; Mantegna, G.; Orlando, C.; Alaimo, A.; Berci, M. A refined aeroelastic beam finite element for the stability analysis of flexible subsonic wings. *Comput. Struct.* **2025**, *307*, 107618. [CrossRef]
22. Böhnisch, N.; Braun, C.; Marzocca, P.; Muscarello, V. Insights into the aeroelastic stability of a wing with distributed electric propulsion systems. *Aerosp. Sci. Technol.* **2026**, *168*, 110763. [CrossRef]

23. Li, S.; Caracoglia, L.; Møller-Madsen, J. Examining adequacy of the empirical Theodorsen function for wind turbine blade section-model aeroelasticity. *J. Fluids Struct.* **2023**, *118*, 103843. [CrossRef]
24. Quero, D. A frequency-domain flutter solver for rotary-wing aeroelasticity. *J. Fluids Struct.* **2025**, *139*, 104435. [CrossRef]
25. Lee, H.; Lee, D.J. Low Reynolds number effects on aerodynamic loads of a small scale wind turbine. *Renew. Energy* **2020**, *154*, 1283–1293. [CrossRef]
26. Epps, B.P.; Roesler, B.T.; Medvitz, R.B.; Choo, Y.; McEntee, J. A viscous vortex lattice method for analysis of cross-flow propellers and turbines. *Renew. Energy* **2019**, *143*, 1035–1052. [CrossRef]
27. Parenteau, M.; Laurendeau, E. A transonic, viscous nonlinear frequency domain Vortex Lattice Method for aeroelastic analyses. *J. Fluids Struct.* **2021**, *107*, 103406. [CrossRef]
28. Tseng, J.B.; Lan, C.E. *Calculation of Aerodynamic Characteristics of Airplane Configurations at High Angles of Attack*; NTRS Author Affiliations Technical Report NASA-CR-4182; NASA: Washington, DC, USA, 1988.
29. Proulx-Cabana, V.; Michon, G.; Laurendeau, E. Parametrization Effects of the Non-Linear Unsteady Vortex Method with Vortex Particle Method for Small Rotor Aerodynamics. *Fluids* **2024**, *9*, 24. [CrossRef]
30. Proulx-Cabana, V. Rapid Non-Linear Computational Algorithms for Rotary-Wing Aeroelasticity. Ph.D. Thesis, Polytechnique Montréal, Montreal, QC, Canada, 2024.
31. Rogowski, K.; Mikkelsen, R.F.; Michna, J.; Wiśniewski, J. Aerodynamic performance analysis of NACA 0018 airfoil at low Reynolds numbers in a low-turbulence wind tunnel. *Adv. Sci. Technol. Res. J.* **2025**, *19*, 136–150. [CrossRef] [PubMed]
32. Dagilis, M.; Lendraitis, M.; Kilikevičius, S. Feasibility of Real-time Aeroelasticity Modeling Using the Unsteady Vortex Lattice Method. In *Proceedings of the AIAA Aviation Forum and Ascend 2025*; American Institute of Aeronautics and Astronautics: Reston, VA, USA, 2025. [CrossRef]
33. Katz, J.; Plotkin, A. *Low-Speed Aerodynamics*, 2nd ed.; Cambridge Aerospace Series; Cambridge University Press: Cambridge, UK, 2001. [CrossRef]

https://doi.org/10.3390/aerospace13080661